Journal of Materials Research and Technology 37 (2025) 231–241

Contents lists available at ScienceDirect

Journal of Materials Research and Technology

journal homepage: www.elsevier.com/locate/jmrt

A novel filament design for improving fused filament fabrication of continuous fiber composites

M. Parker [a,1], S. Norimatsu [b,1], R. Matsuzaki [b,*], D. Arola [a,c,**]

[a] Department of Materials Science and Engineering, University of Washington, Seattle, WA, USA
[b] Department of Mechanical Engineering, Tokyo University of Science, Tokyo, Japan
[c] Department of Mechanical Engineering, University of Washington, Seattle, WA, USA

ARTICLE INFO

Handling Editor: P.Y. Chen

Keywords:
Continuous fibers
Fused filament fabrication
Matrix coating
Reliability
Strength
Interlaminar tensile strength

ABSTRACT

Fused filament fabrication (FFF) of polymer composites with continuous fibers could enable the manufacture of complex structures with exceptionally high specific strength and stiffness. Although filaments with continuous fiber reinforcement are "printable", the fibers undergo damage during printing, leading to reductions in strength and reliability. Of further concern, the printed material generally exhibits low interlaminar tensile strength. In this study, a novel prototype filament for FFF with continuous carbon fibers and polyphenylene sulfide matrix was evaluated for its potential to resist process-related fiber damage introduced during printing and to increase the interlaminar tensile strength. The filament design enrolls a circumferential matrix coating around a fiber reinforced core. According to the measures of strength, the new filament design improved the reliability in axial strength as well as increased the interlaminar tensile strength by over 80 %. While the new coated filament exhibited superior performance overall in the printed condition, it was more sensitive to temperature changes and underwent a substantial decrease in axial tensile strength at $T > 330$ °C due to the decrease in matrix viscosity and consequent reduction in fiber protection. The printability of the new filament design is reported as a function of nozzle temperature, and the mechanisms that cause void formation and fiber damage are discussed.

1. Introduction

There is constant demand for materials that will enable the design and manufacture of engineering structures with improved performance. But the opportunity for fabricating structures from these "advanced" materials depends largely on the availability of manufacturing processes that can accommodate their physical and mechanical properties.

Additive manufacturing (AM) processes, which involve a layer-by-layer approach for the development of components directly from a computer aided model, are often sought for manufacturing structures with new materials. Indeed, AM technologies are now being implemented for near-net-shape manufacturing in industries ranging from aerospace to medicine, as well as in the production of consumer and sporting goods [1–5]. There are many advantages to AM processes, including the ability to minimize material waste, nearly unlimited geometric complexity, as well as design customization [4,6,7]. In addition, components produced by AM can achieve weight saving through custom infill patterns and spatial modulation of the fill density [8,9]. The ability to achieve weight savings without loss of strength or stiffness is a primary goal in the application of fiber reinforced polymers [10]. AM could provide synergistic benefits in the development of structures with composite materials. However, AM of composites has advanced less rapidly than for metal and polymers due to complications in the printing process mechanics, especially for feedstock materials with continuous fiber reinforcements [11–13].

Fused filament fabrication (FFF) is arguably the leading approach for AM of fiber composites [14]. Common matrix materials in this space include polylactic acid (PLA), nylon (PA), and polyethylene terephthalate glycol (PETG); but they potentially suffer from low glass transition and melting temperatures [15]. Semi-crystalline thermoplastics can provide improved thermal and chemical stability, in addition to mechanical properties [15,16]. Polyphenylene sulfide (PPS) is one such candidate with high crystallinity that exhibits superior heat, chemical, and wear resistance [17–19]. Nearly independent of the feedstock

* Corresponding author. Mechanical and Aerospace Engineering, Tokyo University of Science, 2641 Yamazaki, Noda, 278-8510, Chiba, Japan.
** Corresponding author. Materials Science and Engineering, University of Washington, Box 352120, Seattle, WA, 98195-2120, USA.
E-mail addresses: rmatsuza@rs.tus.ac.jp (R. Matsuzaki), darola@uw.edu (D. Arola).
[1] contributed equally to this manuscript and share the first author role.

https://doi.org/10.1016/j.jmrt.2025.05.251
Received 2 March 2025; Received in revised form 17 May 2025; Accepted 30 May 2025
Available online 30 May 2025

selected, there are several printing parameters that universally contribute to final structural properties, including nozzle temperature, environment temperature, print speed, and layer height, among others [20]. These parameters are especially important to the interlayer bond strength, as they contribute to the interfacial adhesion with preceding layers [21–23]. The interlayer (i.e. interlaminar) strength "transverse" to the infill direction is often inferior due to layer-line anomalies and the alignment of defects [24,25]. As the material is extruded and deposited during FFF, pores are generated between the infill lines and contribute to both mechanical anisotropy and inferior transverse mechanical properties [26,27]. However, recent work has shown that the interlayer strength can be improved in FFF by increasing the nozzle temperature, which decreases the interlayer porosity and facilitates more extensive intermingling of polymer chains and entanglement at the layer interfaces [28].

Composite filaments of thermoplastic polymers with fiber reinforcements have been developed for FFF to increase the axial properties [29–32]. While filaments with short fiber reinforcements provide moderate increase in stiffness and strength [33], the largest increase is achieved with continuous fibers. Common reinforcement materials in FFF of composites include carbon fibers (CF), Kevlar, fiberglass, as well as natural fibers such as hemp or jute [34]. A 2019 study investigated the mechanical properties achieved in printing of short and continuous carbon fiber reinforced PA and reported that both fiber loading and infill type/percentage influenced tensile strength [35]. Whereas the addition of short fibers nearly doubled the tensile strength relative to the unreinforced PA, continuous fibers resulted in an order of magnitude increase.

As interest in printing filaments with high strength continuous fiber reinforcement grows, many groups have adopted in-situ nozzle impregnation methods using conventional 3D printers to accelerate materials development. Notably, Matsuzaki et al. improved the tensile strength of PLA by over 400 % with addition of only 6.6 % volume fraction (V_f) of carbon fibers (~42 MPa to 185.2 MPa) [36]. In PEEK (polyetheretherketone), the addition of continuous carbon fiber reinforcement ($V_f \approx 40$ %) increased strength to over 1100 MPa. However, hot isostatic pressing (HIP) treatments were required to overcome the detrimental layerwise porosity and maximize strength, which exceeded 1300 MPa after the consolidation step [37]. As defects in FFF of composites such as fiber clustering and void generation appear problematic [29,35,38] post-printing compaction pressure could serve an important role in improving the integrity of the layer interfaces.

While the axial tensile strength of structures printed by FFF increases with the fiber volume fraction, the reduction in matrix at the intersection of adjacent infill contours poses a challenge to the interlayer bond strength [33,39]. Furthermore, the reduction in matrix that accompanies increasing fiber volume fraction exposes the fibers and raises the potential for fiber damage. Fiber defects resulting from printing of composite filaments with continuous fibers include breakage, wrinkling, twisting, and misalignment from the printing mechanics [40]. Process-related fiber damage reduces the tensile strength and increases property variability [41,42]. These undesired by-products of printing are a fundamental challenge that cannot be reversed in post-processing like polymer defects (such as voids/porosity). Fiber defects appear to be inevitable with current printing technologies and underscore the need for modifications in hardware or feedstock.

Post-processing can be adopted to consolidate the microstructure generated by FFF, but additional post-processing steps are undesirable. Some recent efforts have pursued the development of modified printing systems to overcome fiber damage, and other printing-related defects, including changes in deposition angle and others to alleviate process related stresses [43–45]. Non-planar printing arms and rotating nozzle systems have also been devised for FFF of composite filaments [46,47].

Apart from modifications in printing hardware, other research groups have pursued improvements in microstructure and reduction of printing defects through material selection or parameter optimization. Shuto et al. describe the beneficial changes to deposition shape, void content, and crystallinity in FFF of carbon fiber reinforced PPS that can be achieved via adjustments of nozzle temperature [48]. But it is not clear that temperature alone can improve the interlayer tensile strength sufficiently and reduce printing-related fiber damage.

This investigation explores the potential benefits of a novel filament design for printing continuous fiber composites by FFF, which utilizes a thin circumferential coating of matrix surrounding a core composite filament with continuous carbon fibers. The primary objective of this work was to evaluate the improvements in the printed axial and interlaminar tensile strength achieved by the new prototype design with respect to a conventional composite filament design. Given the importance of printing parameters on shaping the material [49], the microstructure as well as the uniaxial and interlaminar tensile strength were evaluated over a range of nozzle temperatures. Results achieved with the conventional and new composite filament design were compared, and improvements in the printed products discussed.

2. Materials and methods

2.1. Filament

Two generations of continuous carbon fiber reinforced polyphenylene sulfide (CF/PPS) filament designs were evaluated in this investigation. The filaments were developed by Toray Industries, Inc. (Tokyo, Japan) and both utilized Toray T800H–6K–40B carbon fibers and a proprietary PPS matrix. The first-generation filament, which follows a conventional design, contains a 6k CF tow and a nominal fiber volume fraction (V_f) of 40 %, which is denoted CF/PPS. The newly designed second-generation filament applies a secondary pultrusion process to the first-generation filament to deposit an exterior coating (i.e. shell) of the PPS matrix and is referred to as CF/PPS-C (Fig. 1). By virtue of this complimentary process, there is an increase in the filament diameter and decrease in V_f for the CF/PPS-C relative to the conventional filament as outlined in Table 1.

To evaluate the microstructure of the filaments, representative portions of as-received (AR = not-printed) and printed filaments were cross-sectioned, mounted in epoxy (Epofix, Struers, OH, USA) and then polished sequentially with a series of abrasive mesh papers (#800 to #4000). The final steps involved using a cloth pad with alumina polishing slurries of 1 μm and then 0.1 μm particle sizes. Two optical microscopes were used to image the microstructures, including an Olympus BX51M (Olympus Corporation, Center Valley, PA, USA) equipped with a digital camera (1024 x 768 resolution, Olympus SC30), as well as a Keyence digital microscope (VHX-6000, Osaka, Japan). A commercial software (ImageJ, National Institutes of Health, USA) was utilized for image analysis to estimate the void fraction and fiber volume fraction (V_f) through color thresholding, as shown in Fig. 2.

2.2. Printing

A desktop printer (Prusa, Model I3 MK3S, Prague, Czech Republic) for FFF was modified to enable printing of the composite filaments. Specifically, the high melting temperature of the PPS required the use of a high temperature thermocouple and temperature controller as described in Parker et al. [49]. Printing of the filaments was conducted using a range of nozzle temperatures, with all other parameters held constant. Specimens for uniaxial tensile tests were printed with a bed temperature of 90 °C, print speed of 220 mm/min, and a layer height of 0.2 mm. A standard brass nozzle with internal diameter of 1.2 mm was used for all printing.

A 400 mm length of filament was printed onto an elongated steel print bed, partially motorized by a secondary 3D printer to achieve the larger printed lengths required for tensile testing. To aid in adhesion of the printed material to the build plate, a generic hairspray was sprayed directly onto the bed just prior to printing. Five specimens were printed

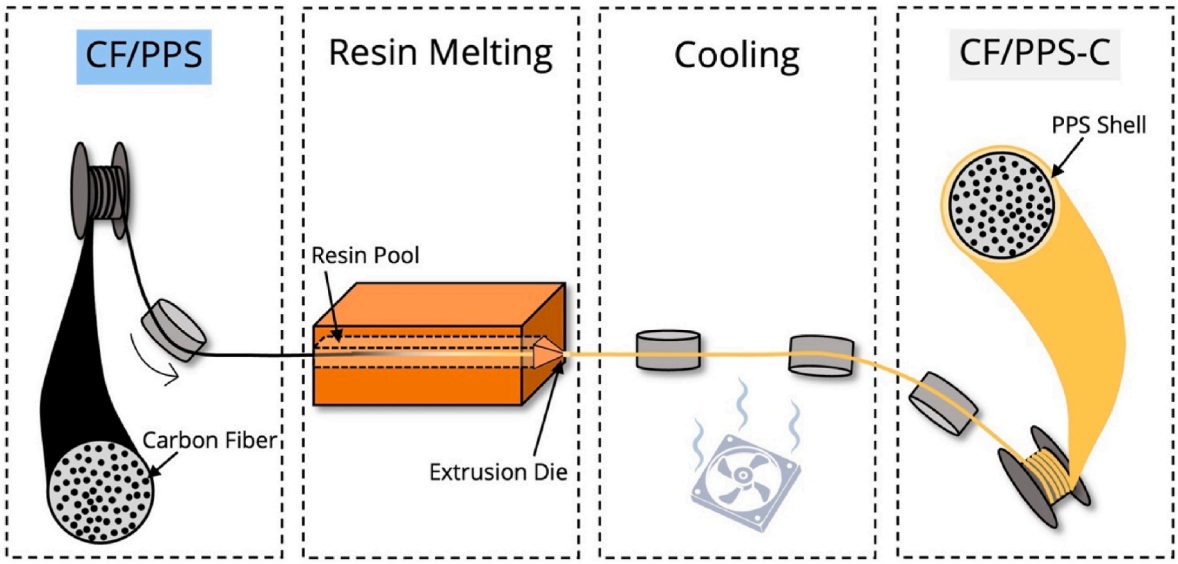

Fig. 1. Schematic representation of the filaments developed for this investigation.

Table 1
Details of the CF/PPS and CF/PPS-C filament properties, including nominal volume fraction and diameter.

	CF/PPS	CF/PPS-C
V_f [%]	40	32
Filament diameter [mm]	0.60	0.64

at each nozzle temperature of 310, 320, 330, and 340 °C for both the CF/PPS and CF/PPS-C filaments. An additional ten specimens were printed at 330 °C and 340 °C of both filament types and compared, for a total of N = 15 at these two temperatures. A corresponding number of AR specimens were cut directly from the spool in 400 mm lengths. The larger number of samples for the two higher temperatures were necessary to support an evaluation of the strength variability.

To evaluate the interlaminar tensile strength of the printed material, rectangular specimens of approximately 3 × 4 cm and consisting of 4 layers were printed according to the print path defined in Fig. 3a. Both the CF/PPS and CF/PPS-C specimens were printed with a layer height of approximately 0.2 mm, for a total thickness of just under 1 mm, and with the entire printed path consisting of continuous deposition of the filament as shown in Fig. 3b. The specimens were printed on a steel bed set to 115 °C (to facilitate improved bed adhesion with longer print times) with a print speed of 220 mm/min. The conventional and coated filaments were printed with a pitch width of 0.8 mm and 0.9 mm, respectively; the difference was necessary to accommodate the difference in filament diameters. For a more detailed investigation, printing of these specimens was performed at nozzle temperatures from 310 to 330 °C, at intervals of 5 °C. The reduced range in temperatures was guided by results of the axial testing, which suggested that printing at 340 °C was less desirable. Printing was performed to obtain multiple CF/PPS (N = 5) and CF/PPS-C (N = 3) specimens for each temperature. A smaller number of specimens were produced with the coated filament due to limitations posed by the total volume of material available.

2.3. Mechanical testing

Uniaxial tensile testing of the as-received and printed filament sections was performed using an Instron testing frame (Model E1000, Norwood, MA, USA) equipped with a 2.5 kN load cell and custom fixtures as shown in Fig. 4a [49]. Both ends of the specimen were sandwiched between a layer of sandpaper and a small aluminum plate secured with clamps. The gauge length was roughly 90 mm for each sample, and a loading rate of 1 mm/min was used, for an effective strain rate of ~0.01 s^{-1}. Acquisition of the load and displacement was performed at a rate of 1 Hz. Three measurements of diameter or width and thickness were taken around the center of the gage length to estimate the average diameter and cross-sectional area. The load responses were recorded and used to determine the engineering stress and calculate the ultimate tensile strength (UTS).

In addition to the deterministic approach to strength assessment, the two-parameter Weibull distribution was used to further evaluate and compare the ultimate strength measurements resulting from axial testing of the filaments to failure. The statistical distribution in the ultimate load to failure was also assessed using this approach. For strength, the probability distributions for failure are described according to

$$P_f = 1 - exp\left(- \left(\frac{\sigma}{\sigma_\circ}\right)^m \right) \quad (1)$$

where P_f represents the probability of failure at the axial stress (σ), m is the Weibull modulus, and σ_o is the characteristic strength. The probability function for failure (P_f) was defined according to median rank estimate according to

$$P = \frac{Stress\ Rank - 0.3}{Number\ of\ Samples - 0.4} \quad (3)$$

In evaluation of the ultimate load to failure distributions, equation (1) was defined in terms of the load at failure (L), the characteristic critical load (L_o) and the Weibull modulus (m). Fifteen tensile samples of each printed configuration were evaluated and used in constructing the Weibull diagrams describing the probability of failure distributions for stress and load.

To determine the interlaminar tensile strength (ILTS), tensile tests were performed on planar specimens of printed laminate using a Shimadzu universal testing machine (Autograph AGS-J, 10 kN, Kyoto, Japan) according to the arrangement shown in Fig. 4b. The printed 4-layer laminate specimens were bonded to aluminum tabs with dimensions of 15 × 20 mm with a small amount of epoxy resin adhesive (Cemedine Hi-Super 30, Tokyo, Japan). Once the adhesive set, excess portions of the composite specimens that exceeded the dimensions of the tabs were removed, which were largely the edges of the printed 4-layer laminates, including the turning points. The aluminum blocks were introduced within the pin fixtures in the load frame (Fig. 4b) such that

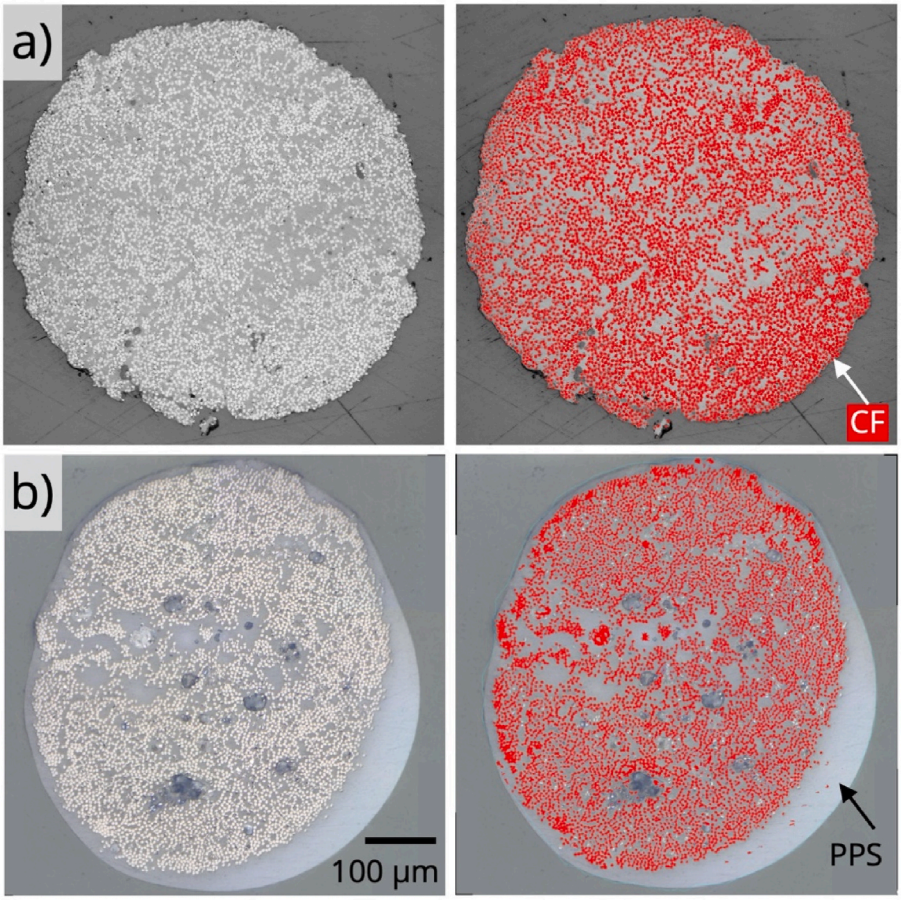

Fig. 2. Cross-sectional views of the a) CF/PPS and b) CF/PPS-C filaments with overlay of digital fiber detection. Note that the exterior matrix shell thickness in (b) is not symmetric, which is a representative image of the worst-case distribution. The coating ranged from being completely uniform to unsymmetric.

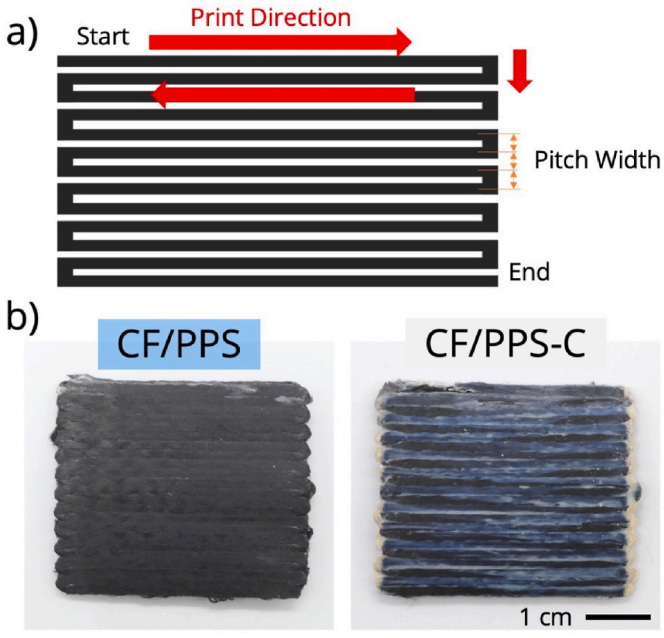

Fig. 3. Details of the interlaminar tensile strength specimens. a) The continuous print path for a layer, and b) representative multi-layer specimens of CF/PPS and CF/PPS-C.

the layers were oriented perpendicular to the axis of applied force; the specimens were loaded to failure with a loading rate of 1.0 mm/min. The interlaminar tensile strength was calculated in terms of the ratio of maximum force to the cross-section area of the specimens.

A one-way ANOVA was used to compare axial load and stress measurements for the samples printed with the conventional and coated filaments. The same analysis was also employed for the interlaminar tensile strength. Significant differences were identified by a value of $p \leq 0.05$.

2.4. Microstructural analysis

Scanning electron microscopy (SEM) was performed on sacrificial printed specimens that were prepared for uniaxial tension experiments using a Phillips Model XL30 (Philips/FEI Company, Lausanne, Switzerland). For both the CF/PPS and CF/PPS-C filaments, the specimens were printed, and a 1 cm section was cut from approximately the center of the strand. The extracted specimens were sputter coated with a 4 nm layer of platinum and imaged at a beam accelerating voltage of 5 kV over a range of magnifications.

For the multi-layer printed specimens of CF/PPS and CF/PPS-C, five cross sections were prepared from randomly selected specimens and a collection of images were acquired. Area measurements were made through color thresholding in ImageJ, which revealed the discrete fibers, voids, and overall filament according to their grayscale values. Due to potential variations in the image analysis related to user methodology and subjectivity, a single individual performed all the image analysis for repeatability. The void percentage was estimated from these images according to the ratio of the void area to the region of interest area and is

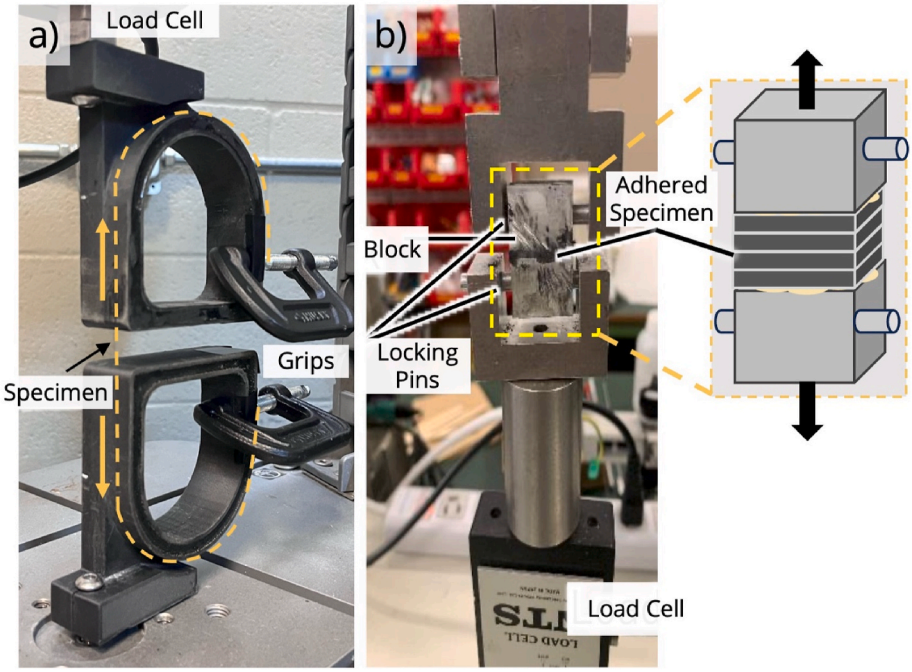

Fig. 4. Experimental arrangements for a) uniaxial tensile testing, and b) interlaminar tensile strength testing of the printed specimens (Not to scale).

expressed according to

$$Void\ fraction\ [\%] = \frac{Void\ area\ [\mu m^2]}{Extraction\ area\ [\mu m^2]} \times 100 \quad (4)$$

A method for evaluating the filament area fraction (A_f) of the printed filaments was applied to account for the deviation of the cross-section from an ideal rectangle. The filament area fraction was then estimated according to the ratio of the filament area to the area of an ideal rectangle according to

$$Filament\ area\ fraction = \frac{Filament\ area}{Rectangular\ area} \quad (5)$$

Measurements were taken at five random sections taken from the first layer of the CF/PPS and CF/PPS-C specimens at each nozzle temperature.

3. Results and discussion

A prototype filament design was conceived to overcome two challenges in FFF of continuous fiber reinforced polymers, namely: i) the process-related fiber damage that is incurred during printing filaments with continuous fibers [41,42], and ii) the traditionally low interlaminar tensile strength of composites with thermoplastic matrix [33,34]. Previous reported work has shown that the CF/PPS with high V_f has higher strength, as well as lower variability in axial strength than commercial filaments with continuous fibers [42].

3.1. Uniaxial tensile strength

Representative stress-strain curves are presented for each filament design in Fig. 5 for the AR condition, i.e., prior to printing, and after being printed at 330 °C. The filaments exhibited linear-elastic behavior to failure with strain at fracture below 1.5 %. Failure of the filaments reflected brittle fiber-dominated behavior, as expected. The reduction in strength due to printing is clearly apparent with respect to the AR condition in Fig. 5.

The average ultimate tensile strength (UTS) of the CF/PPS and CF/PPS-C filaments are presented in Table 2. Results are presented for the

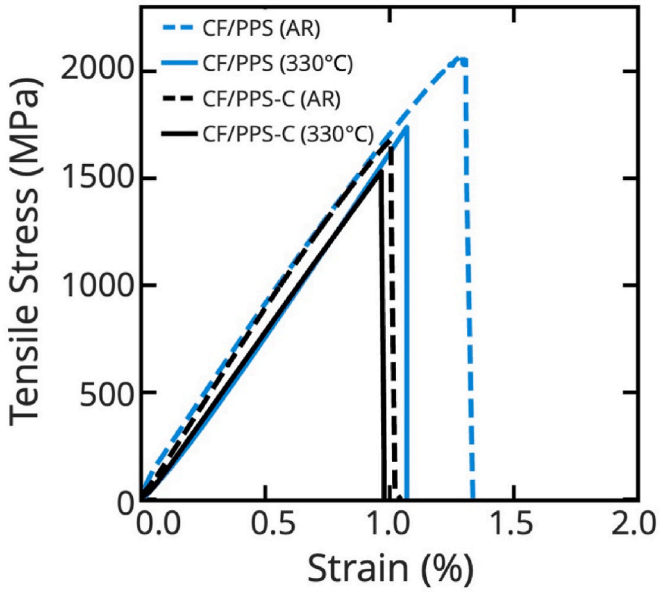

Fig. 5. Axial stress-strain responses of selected filaments in the as-received and printed condition at 330 °C. Note the reduction in strength after printing relative to the AR condition.

Table 2
Average ultimate tensile strength (UTS) and ultimate load (UL) of the CF/PPS and CF/PPS-C filaments.

	UTS [MPa]			UL [N]		
Filament	AR	310 °C	340 °C	AR	310 °C	340 °C
CF/PPS	2036 ± 71	1851 ± 100	1946 ± 61	543 ± 17	506 ± 20	564 ± 20
CF/PPS-C	1681 ± 40	1411 ± 194	1300 ± 179	538 ± 15	494 ± 74	453 ± 52

as-received (AR) condition and in the printed conditions corresponding to the minimum and maximum nozzle temperature. In the AR condition, the CF/PPS and CF/PPS-C filaments achieved an UTS of 2036 ± 71 MPa and 1681 ± 40 MPa, respectively, which exceeds reported values for comparable commercial composites [33,50]. The strength of both the CF/PPS and CF/PPS-C filaments was reduced by printing, with overall average reductions ranging from 4 to 22 %, depending on printing temperature. The reduction in printed strength of the CF/PPS-C filament was lower than that for the CF/PPS over the range in printing temperatures, with an exception at 340 °C. At that temperature there was a marked reduction in axial strength of the CF/PPS-C, which requires further discussion.

The distribution in UTS of the printed filaments is shown as a function of nozzle temperatures in Fig. 6a. Of note, the UTS of the printed materials was lower than the AR state, whereas the range in UTS was greater. The differences in UTS between the CF/PPS and CF/PPS-C were significant at all temperatures ($p \leq 0.05$), which is expected from the lower V_f of the CF/PPS-C. While the UTS of the CF/PPS remained largely constant over the range in nozzle temperature, the highest UTS (1946 ± 61 MPa) resulted from printing at 340 °C. Interestingly, the highest UTS (1579 ± 35 MPa) of the CF/PPS-C resulted from printing at 330 °C, with notable reduction in strength and greater variability with increase to 340 °C.

The lower UTS of the CF/PPS-C relative to the uncoated filament in the unprinted condition results from the lower global fiber V_f of the coated filament (Table 1) and larger cross-sectional area. Due to the consistency in number of fibers of the two filament designs, the ultimate tensile load (UL) at failure serves as an alternate and more objective means of comparing the material performance. The distribution in the UL of the printed filaments is shown as a function of nozzle temperatures in Fig. 6b. The average UL to failure of the CF/PPS and CF/PPS-C filaments in the AR condition were 543 ± 17 and 538 ± 15 N, respectively, which were not significantly different ($p > 0.05$). This consistency in the as-received UL responses (Table 2), which depends primarily on the carbon fiber tow, indicates that the additional processing required to apply the matrix coating of the CF/PPS-C did not induce fiber damage. As evident in Fig. 6b, the UL responses for the two filament designs were not significantly different ($p > 0.05$), except at 340 °C. For instance, at 330 °C the ULs were 538 N and 539 N for the CF/PPS and CF/PPS-C, respectively, which are consistent with the values prior to printing (Table 2). Therefore, the exterior matrix coating offers some protection to the fibers during printing and did not decrease the strength or load to failure.

To further understand the influence of coating and printing temperature, the Weibull distribution for both the UTS and UL responses were obtained for the CF/PPS and CF/PPS-C filaments and are presented for printing at 330 °C and 340 °C in Fig. 6c–d; results for the AR condition are also presented for comparison. The sample size was increased from N = 5 to N = 15 to support the Weibull statistics. Regarding strength, there is a clear decrease in UTS and increase in its variability for both filaments after printing. The latter is reflected by a reduction in the Weibull modulus (i.e., the slope of the distributions) after printing. For the CF/PPS, the Weibull modulus for the UTS in the AR condition is 32, which decreases to 11 at printing temperatures 330 and 340 °C. Conversely, for the CF/PPS-C the modulus for the AR condition is 47, and decreases to 35 at 330 °C and then further to 11 at 340 °C. While the CF/PPS has a higher characteristic strength at 330 °C, the CF/PPS-C has higher Weibull modulus indicating greater consistency and reliability. The substantial reduction in Weibull modulus of the CF/PPS-C with increase to 340 °C highlights its sensitivity to changes in the printing mechanics that result from elevated temperatures.

Regarding the UL distributions for the CF/PPS and CF/PPS-C filaments in Fig. 6d, prior to printing they are essentially identical, as expected, with a Weibull modulus of 33 and 36, respectively. After printing at 330 °C, there is a reduction in the Weibull modulus with respect to the as-received condition, decreasing to 18 and 27, respectively without and with the coating. Hence, akin to the strength measurements, the CF/PPS-C exhibits greater consistency in the UL to failure. However, at 340 °C the moduli decrease further to 12 and 18, respectively. This sharp reduction suggests that at 340 °C there is a change in the printing mechanics that facilitated fiber damage. Additionally, by evaluating the Weibull distribution for load of the CF/PPS-C

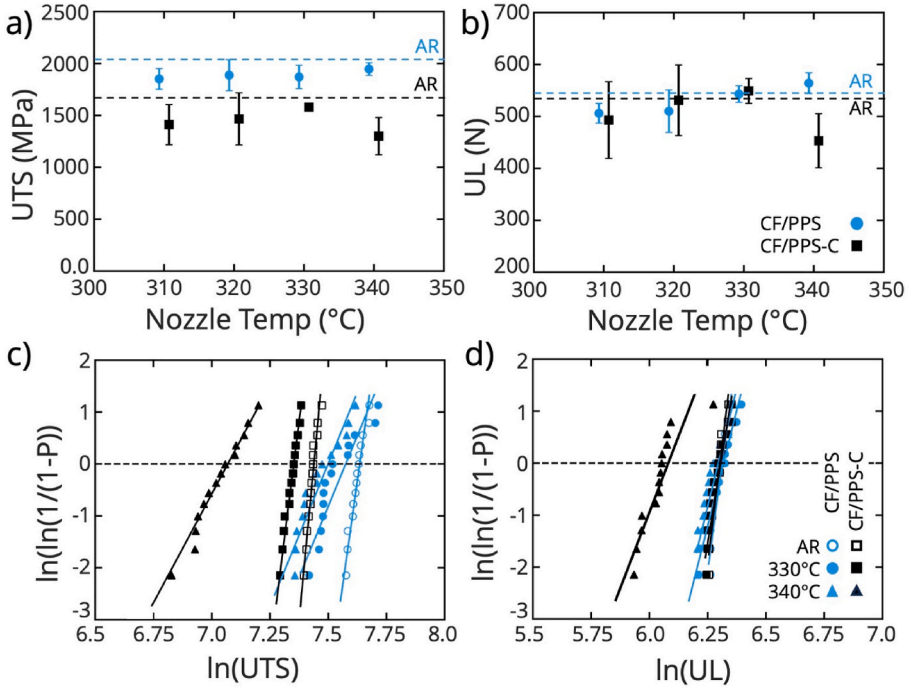

Fig. 6. Comparison of the a) UTS and b) UL as a function of nozzle temperature for the CF/PPS and CF/PPS-C filaments in the printed condition (temperature values are slightly offset at each condition for the sake of visual clarity). Dashed lines in (a,b) represent the average property of the as-received (AR) filament (not printed). Comparisons of the Weibull distributions for filaments in the AR and printed conditions for the c) UTS and d) UL.

at 340 °C (Fig. 6d), there are substantial outliers at both ends of the distribution, thereby suggesting multiple root causes of failure. It is hypothesized that the increase to 340 °C decreased the PPS viscosity such that it reduced its ability to protect the surface fibers. Damage then occurred to the peripheral fibers and the UTS and UL were reduced accordingly due to fiber breakage. It is also important to highlight that the coating increased the diameter of the filaments by nearly 10 %. Since the same nozzle diameter was used for printing both filaments, the contact forces between the nozzle body and the CF/PPS-C filament undoubtedly increased, which increases the potential for damage.

3.2. Interlaminar tensile strength

Based on the marked reduction in axial strength at 340 °C, the ILTS was evaluated over the range in printing temperature from 310 °C to 330 °C. The ILTS test format, a modified form of the Japanese Industrial Standard K6849 and ISO 6922:1987, was key to assessing the contribution of the peripheral matrix coating of the CF/PPS-C filament in a multi-layer printed structure. The ILTS distributions for the two generations of filaments are shown over this temperature range in Fig. 7. Overall, the maximum average ILTS was 1.55 MPa ± 0.6 and resulted from the CF/PPS-C printed at the highest temperature. The ILTS of the coated filament increased to nearly twice that achieved by the CF/PPS filament and represented a significant increase. Nevertheless, the overall ILTS was modest; low interlaminar strength is a ubiquitous problem in FFF of thermoplastics [51]. As filaments with continuous fiber reinforcements have even less matrix for interlayer bonding, they are incredibly susceptible to this phenomenon. It is important to highlight that the ILTS values obtained here are comparable with those reported for other continuous fiber composites produced by FFF [33,52]. Despite the increase achieved with matrix coating, the ILTS is only a fraction of the PPS tensile strength, which is roughly 61 MPa as obtained through printing of tensile bars (N = 4).

The ILTS responses for both the CF/PPS and CF/PPS-C filaments exhibited convex distributions over the printed temperature range; the highest values were obtained at the maximum temperature. The differences between CF/PPS and CF/PPS-C are statistically significant across the entire temperature range. The variability in ILTS, especially, in CF/PPS-C, reflects that filament printability is sensitive to small changes in temperature, which was also observed in the uniaxial results in Fig. 6a–b. The comparatively large deviation in the CF/PPS-C at 325–330 °C could be due to the removal of excess matrix from the trailing edge of the filament through contact with the nozzle interior edge, which reduces the matrix available for interlayer bonding. Of note, Seon et al. applied this method of interlaminar testing and commented that while valuable, there are challenges related to its sensitivity to manufacturing defects such as voids/porosity, etc. [51]. Clearly the matrix coating applied to the CF/PPS-C was helpful. However, the additional matrix was not sufficient to produce a fully contiguous and well-integrated interface that is resistant to defects, and continued efforts to increase interlaminar bonding are needed.

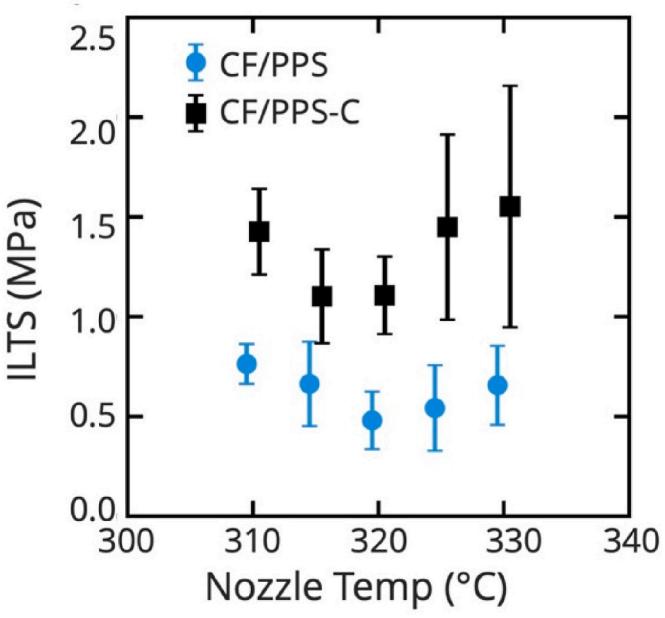

Fig. 7. Interlaminar tensile strength (ILTS) of the CF/PPS and CF/PPS-C filaments after printing as a function of nozzle temperature.

3.3. Printed filament characteristics

Results for the axial and interlaminar strength measurements exhibited an undesirable degree of variation. Hence, the printed filaments were evaluated using both optical and scanning electron microscopy to assess potential contributions to the variations. A comparison of the printed CF/PPS and CF/PPS-C filaments is shown in Fig. 8 from two perspectives. Specifically, representative segments of the top and bottom faces of the filaments are shown in Fig. 8a and c, and Fig. 8b and d, respectively. The full width of the printed filament is shown in these frames and the bottom surface refers to that contacting the build plate or previously printed layer. In each filament, a portion of carbon fibers is fully exposed on the top surface, whereas the bottom surface is largely covered with a thin layer of PPS matrix, albeit some fibers are still visible. A few fractured fibers are exposed and visible at the sides of the specimens. Akin to features of the uncoated filament, the top surface of the printed CF/PPS-C exhibits exposed fibers with limited matrix (Fig. 8c). In comparison, the extent of matrix on the bottom surface of the coated filament appears thicker (Fig. 8d) than for the uncoated filament (Fig. 8b). There is also a larger deposit of PPS on the sides of the specimens, which is most apparent on the top surface of the CF/PPS-C in Fig. 8c. Regardless of these observations, an evaluation of the printed CF/PPS-C showed no evidence of an interface between the filament core and shell; the filament appeared as a single cohesive unit, with no cracking or interfacial voids.

It appears that concentrated shear contact between the filament and nozzle removed matrix from the top surface (i.e. the trailing edge), which exposed fibers to damage. This can also be seen in Fig. 3b, where the added matrix is inconsistently spread on the surface and pooled at the turning points. Regardless of printing temperature, exposed carbon fibers are evident on the printed surface of both CF/PPS and CF/PPS-C that are not aligned with the filament and exhibit some degree of waviness.

3.4. Voids and area faction in multi-layer printing

To further understand the ILTS results, the void and fiber area fractions were evaluated from sectioned multi-layer specimens. Visible defects in the microstructure are believed to arise from: i) the high stiffness of the reinforced filament with limited matrix that does not readily conform well to the previous layer, ii) the stochastic nature of reinforcement distribution at deposition, and iii) the limited matrix to fill gaps. A representative cross-section of a specimen printed with CF/PPS filament at 315 °C is shown in Fig. 9a. The cross-section reveals multiple large voids along the layer interfaces as highlighted, in addition to many small voids. Based on the overall shape of the individual layers there are substantial irregularities that are apparent over the range in temperatures. In some cases, small bundles of carbon fibers are dislodged from the main print body, as seen at the top of the sample in Fig. 9b. At 330 °C, voids of similar size and shape are evident in the printed specimens of both filaments (Fig. 9c–d). While large voids are observed in the CF/PPS-C specimens at all temperatures, they appear to be less irregular in shape than those produced in printing the CF/PPS filament.

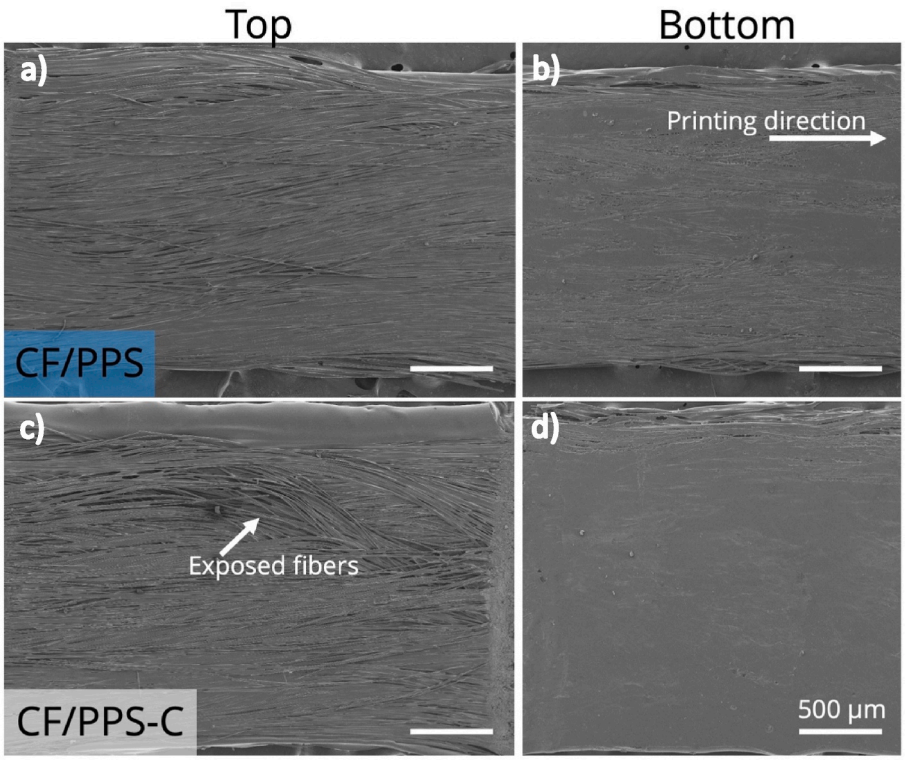

Fig. 8. SEM views of the top surface and bottom surface of CF/PPS and CF/PPS-C filaments printed at 320 °C. a,b) top and bottom surfaces of the printed CF/PPS filament, respectively. c,d) Top and bottom surfaces of the printed CF/PPS-C filament, respectively. The bottom surface contacts the print bed after exiting the nozzle and the top surface is exposed for the next layer.

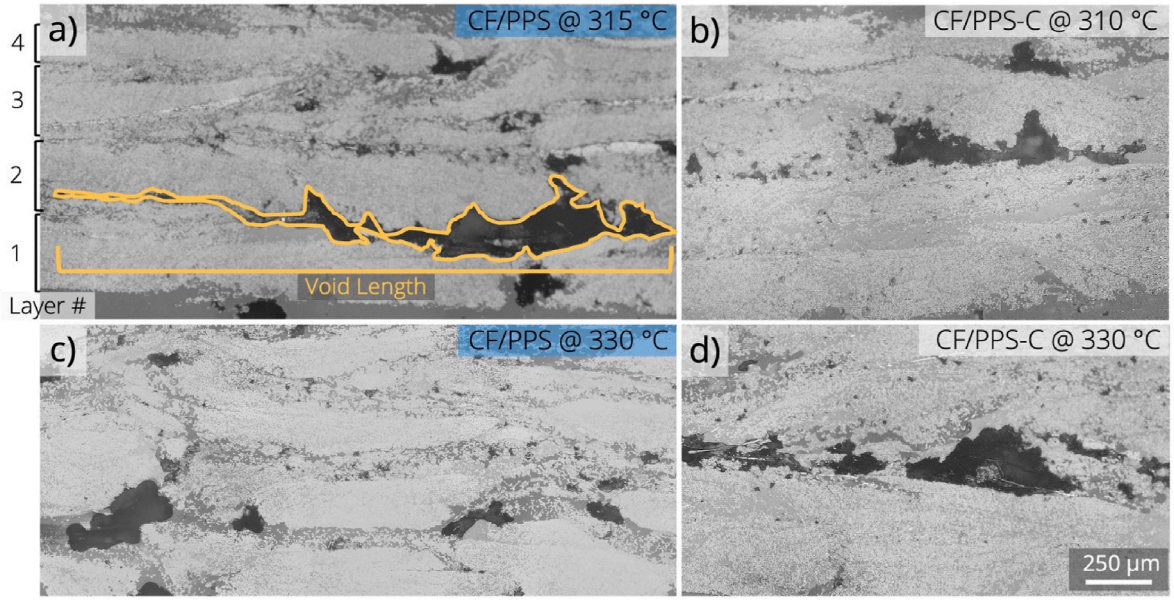

Fig. 9. Evaluation of the void characteristics and their distribution in CF/PPS at a) 315 °C and c) 330 °C and for the CF/PPS-C at b) 310 °C and d) 330 °C.

Overall, the CF/PPS printed materials appear to have more interlayer defects relative to the CF/PPS-C. The PPS crystallinity is sensitive to rate of heating and cooling [53,54], which could contribute to bonding between the layers and resulting mechanical properties. Therefore, identifying the ideal print temperature should be performed and take into consideration the thermal behavior of both the matrix and reinforcement, to maximize interlayer adhesion. Nevertheless, the major contribution to the weak interlaminar strength is the large voids present at the layer interface (Fig. 9).

The relationship between nozzle temperature and void characteristics are shown in Fig. 10. As shown in Fig. 10a, the average void area fraction ranged from roughly 5–8 % for both filaments. There is no distinct trend between the void content and nozzle temperature. Surprisingly, there was no significant difference between the CF/PPS and –C filaments ($p > 0.05$). Yet, the lowest void content overall was achieved by the CF/PPS-C filament printed at the intermediate temperatures. The

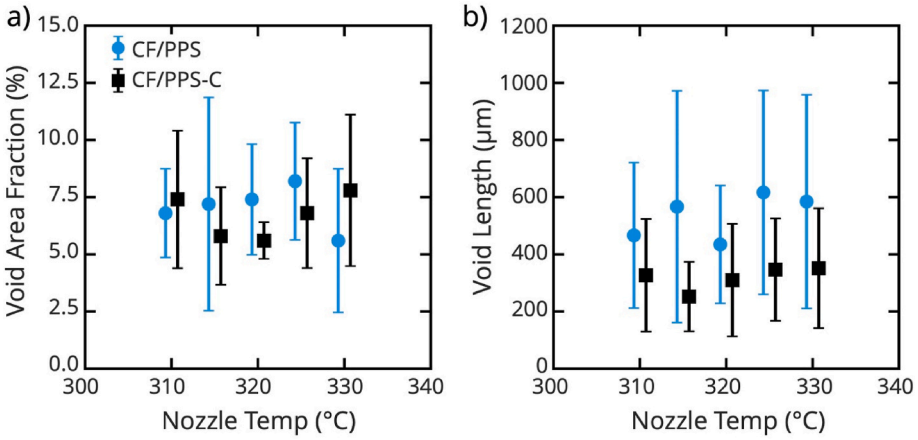

Fig. 10. Detailed measures of the a) void ratio and b) transverse void length in the CF/PPS and CF/PPS-C materials, as a function of nozzle temperature.

average void length measurements at the interface range from roughly 250 to over 600 μm (Fig. 10b) and are significantly different ($p \leq 0.05$) at all temperatures. In comparing void lengths, the laminates printed with the CF/PPS-C filaments had shorter lengths overall, with range from 250 to 350 μm. Clearly, the additional coating of the CF/PPS-C provided more interfacial contact and reduced void length as seen in Fig. 10a. Nevertheless, the matrix coating was insufficient to overcome the stochastic aspect of reinforcement and laminate layer surface topography. Further improvements of the interlaminar strength in printing of continuous fiber composites will require control of this aspect of the microstructure. Adding more matrix coating could be a solution, but at the cost of lower V_f and apparent axial strength.

The deposited filament was evaluated in terms of the filament area fraction (A_f) as shown in Fig. 11a, which represents a measure of geometry with respect to an ideal rectangular deposition. The area fraction distribution of the printed filament in terms of the printing temperature is shown in Fig. 11b. Interestingly, both filaments exhibit the largest values of A_f at 310 °C and 330 °C, and the smallest value at the intermediate temperatures. Overall, the printed CF/PPS-C filament has larger A_f, or a more ideal deposition shape than that for the CF/PPS at all temperatures. Furthermore, a comparison of the ILTS in Fig. 7 with the A_f in Fig. 11 show that the ILTS is highly correlated with the A_f and that the strength increased with area fraction. The correlation coefficients between A_f and the ILTS are 0.96 and 0.91 for the for CF/PPS and CF/PPS-C filaments, respectively. Thus, printing temperature controlled the deposited shape of the filament, which contributed to the area fraction and strength. The larger area fraction of the CF/PPS-C filament is a principal contributor to the higher ILTS of that material. When printing larger multilayer structures, the shape, size, and location of the voids are all contributors. Longer void lengths are more likely to facilitate delamination, leading to lower strength in the direction of the plate thickness. And while smaller interfacial voids are less likely to influence the interlaminar strength, they can influence other properties, especially under cyclic loading.

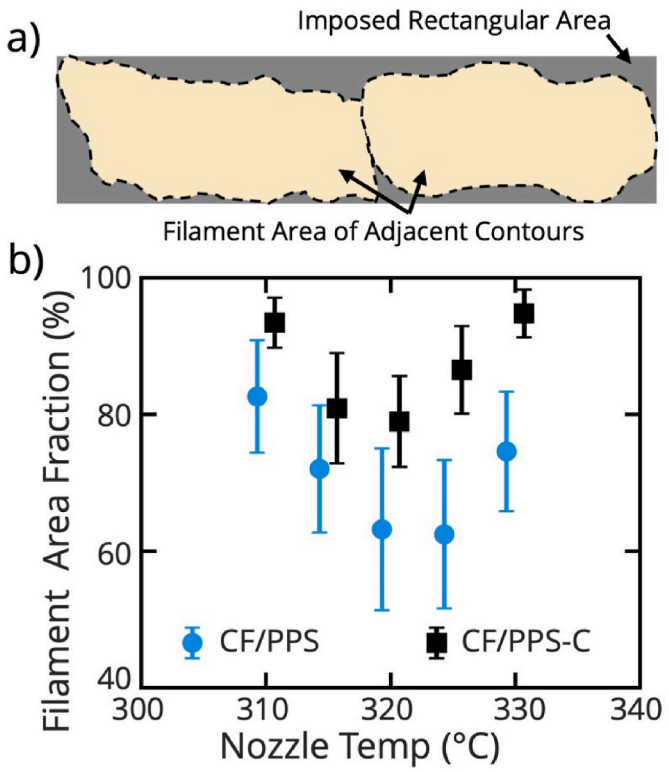

Fig. 11. Printed filament area fraction measurements. a) Definitions of area used in estimating the filament area fraction, and b) area fraction distribution as a function of printing temperature in CF/PPS and CF/PPS-C.

Results of this investigation have shown that a simple modification of the conventional filament design could help improve the commercial potential for FFF of continuous fiber composites. Through fundamental mechanical testing and microstructural evaluation, an important aspect of process mechanics related to printing temperature was elucidated, and an optimum of 330 °C was identified. Results showed that the new filament design with exterior coating has potential to improve the printed material durability, but that printing temperature must be tightly controlled. While the ILTS was improved by 2X, it remains much lower than desired. A key question remains: how could changes to the printer hardware or the filament design promote a higher quality and stronger interface? Future efforts should be focused on evaluating the printed layer topography to reveal deviations from uniformity, and micro-computed tomography to examine and further quantify interfacial voids. Additional methods of structural evaluation could be useful, including flexural tests and interlaminar shear testing to help better understand the influence of interfacial morphology on the microstructure and resulting mechanical properties.

There are additional limitations to the study that should be considered. For instance, the nozzle geometry was not adjusted for the larger diameter of the CF/PPS-C filaments and could have contribute to removal of the surface matrix during printing. Additional aspects of nozzle geometry and printing parameters could be explored to adjust the nozzle/filament contact and ironing pressure applied to the deposited filament by the nozzle. Lastly, the matrix coating of the prototype CF/PPS-C filament was not consistently symmetric (Fig. 2), and only a single matrix coating thickness was used. The importance of these factors and potential improvements should be explored in future studies.

4. Conclusion

An experimental investigation was performed to evaluate the printability of a new filament design for Fused Filament Fabrication (FFF) of continuous fiber composites. The new design consists of a conventional core of carbon fibers and polyphenylene sulfide matrix (CF/PPS) with complimentary exterior matrix coating (CF/PPS-C). This design was conceived to reduce fiber damage and increase both the axial and interlaminar tensile strength (ILTS) of the printed material. The strengths were evaluated over printing temperatures that ranged from 310 to 340 °C. Results showed that the exterior matrix skirt served to protect the fibers, as well as improve the interface bonding strength between layers due to the increased matrix content. Weibull statistics showed that the coating (CF/PPS-C) improved the axial properties through reduced fiber damage, with reliability approaching that of the as-received (unprinted) condition. The coating also nearly doubled the ILTS. However, the new design underwent a significant decrease in tensile strength at the highest temperature (340 °C) due to the reduction in matrix viscosity and loss of fiber protection. Overall, the results show that the addition of an exterior matrix skirt can increase the strength and reliability of components produced by FFF with continuous fiber composites. However, surface damage to the fibers and interfacial voids between layers are prevailing issues in printing filaments with high volume fraction fibers, and will require further effort to overcome.

Declaration of competing interest

The authors declare that they have no known competing financial interests or personal relationships that could have appeared to influence the work reported in this paper.

Acknowledgements

The authors acknowledge that this work was partially supported by a grant from the Joint Center for Aerospace Technology Innovation (JCATI; PI Arola). M. Parker was partially supported by a scholarship from the National Science Foundation SSTEM program, DUE #1800968 (PI Arola). The authors gratefully acknowledge Toray Industries, Inc., Japan, for their supply of materials and technical advice that made this investigation possible. Part of this work was conducted at the Molecular Analysis Facility, a National Nanotechnology Coordinated Infrastructure (NNCI) site at the University of Washington, which is supported in part by funds from the National Science Foundation (awards NNCI-2025489, NNCI-1542101), the Molecular Engineering & Sciences Institute, and the Clean Energy Institute.

Appendix A. Supplementary data

Supplementary data to this article can be found online at https://doi.org/10.1016/j.jmrt.2025.05.251.

References

[1] Blakey-Milner B, Gradl P, Snedden G, Brooks M, Pitot J, Lopez E, Leary M, et al. Metal additive manufacturing in aerospace: a review. Mater Des 2021;209:110008. https://doi.org/10.1016/j.matdes.2021.110008.
[2] Lakkala P, Munnangi SR, Bandari S, Repka M. Additive manufacturing technologies with emphasis on stereolithography 3D printing in pharmaceutical and medical applications: a review. Int J Pharm: X 2023;5:100159. https://doi.org/10.1016/j.ijpx.2023.100159.
[3] Garg M, Rani R, Meena VK, Singh S. Significance of 3D printing for a sustainable environment. Mater Today Sustainability 2023;23:100419. https://doi.org/10.1016/j.mtsust.2023.100419.
[4] Jadhav A, Jadhav V. A review on 3D printing: an additive manufacturing technology. Mater Today Proc 2022;62:2094–9. https://doi.org/10.1016/j.matpr.2022.02.558.
[5] Dai S, Zhu K, Wang S, Deng Z. Additively manufactured materials: a critical review on their anisotropic mechanical properties and modeling methods. J Manuf Processes 2025;141:789–814. https://doi.org/10.1016/j.jmapro.2025.02.038.
[6] Nazir A, Gokcekaya O, Billah KM, Ertugrul O, Jiang J, Sun J, et al. Multi-material additive manufacturing: a systematic review of design, properties, applications, challenges, and 3D printing of materials and cellular metamaterials. Mater Des 2023;226:111661. https://doi.org/10.1016/j.matdes.2023.111661.
[7] Praveena BA, Lokesh N, Abdulrajak B, Santhosh N, Praveeba BI, Vignesh R. A comprehensive review of emerging additive manufacturing (3D printing technology): methods, materials, applications, challenges, trends and future potential. Mater Today Proc 2022;52:1309–13. https://doi.org/10.1016/j.matpr.2021.11.059.
[8] Heitkamp T, Kuschmitz S, Girnth S, Waldt N, Klawitter G, et al. Design principles and restrictions for continuous fiber-reinforced additive manufacturing. J Mech Des 2024;146(6):062002. https://doi.org/10.1115/1.4065142.
[9] Khan N, Riccio A. A systematic review of design for additive manufacturing of aerospace lattice structures: current trends and future directions. Prog Aerosp Sci 2024;149:101021. https://doi.org/10.1016/j.paerosci.2024.101021.
[10] Gairola S, Jayaganthan R. Lattice infill strategies for topology optimisation towards achieving lightweight designs for additive manufacturing: structural integrity, and manufacturing consideration. J Manuf Processes 2025;139:224–38. https://doi.org/10.1016/j.jmapro.2025.01.047.
[11] Zhuo P, Li S, Ashcroft IA, Jones AI. Material extrusion additive manufacturing of continuous fibre reinforced polymer matrix composites: a review and outlook. Composites Part B 2021;224:109143. https://doi.org/10.1016/j.compositesb.2021.109143.
[12] Yuan S, Li S, Zhu J, Tang Y. Additive manufacturing of polymeric composites from material processing to structural design. Composites Part B 2021;219:108903. https://doi.org/10.1016/j.compositesb.2021.108903.
[13] Zhang K, Zhang H, Wu J, Chen J, Yang D. Improved fibre placement in filament-based 3D printing of continuous carbon fibre reinforced thermoplastic composites. Composites, Part A 2023;168:107454. https://doi.org/10.1016/j.compositesa.2023.107454.
[14] Parandoush P, Lin D. A review on additive manufacturing of polymer-fiber composites. Compos Struct 2017;182:36–53. https://doi.org/10.1016/j.compstruct.2017.08.088.
[15] Shanmugam V, Babu K, Kannan G, Mensah RA, Samantaray SK, Das O. The thermal properties of FDM printed polymeric materials: a review. Polym Degrad Stab 2024;228:110902. https://doi.org/10.1016/j.polymdegradstab.2024.110902.
[16] Makki T, Vattathurvalappil SH, Theravalappil R, Nazir A, Alhajeri A, Azeem MA, et al. 3D and 4D printing: a review of virgin polymers used in fused deposition modeling. Composites. Part C 2024;14:100472. https://doi.org/10.1016/j.jcomc.2024.100472.
[17] Pan S, Shen H, Zhang L. Effect of carbon nanotube on thermal, tribological and mechanical properties of 3D printing polyphenylene sulfide. Addit Manuf 2021;47:102247. https://doi.org/10.1016/j.addma.2021.102247.
[18] Yeole P, Hassen AA, Kim S, Lindahl J, Kunc V, Franc A, et al. Mechanical characterization of high-temperature carbon fiber-polyphenylene sulfide composites for large area extrusion deposition additive manufacturing. Addit Manuf 2020;34:101255. https://doi.org/10.1016/j.addma.2020.101255.
[19] Hao P, Li Y, Huan D, Wang Z, Xiao J. Exploration of process parameters and post-processing of 3D printed SCF/PPS for low-altitude aircraft fabrication. Aerospace Traffic and Safety 2025. https://doi.org/10.1016/j.aets.2024.12.008.
[20] Gao X, Qi S, Kuang X, Su Y, Li J, Wang D. Fused filament fabrication of polymer materials: a review of interlayer bond. Addit Manuf 2021;37:101658. https://doi.org/10.1016/j.addma.2020.101658.
[21] Blok LG, Yu H, Woods BKS. An investigation into 3D printing of fibre reinforced thermoplastic composites. Addit Manuf 2018;22:176–86. https://doi.org/10.1016/j.addma.2018.04.039.
[22] Pulipaka A, Gide KM, Beheshti A, Bagheri ZS. Effect of 3D printing process parameters on surface and mechanical properties of FFF-printed PEEK. J Manuf Processes 2023;85:368–86. https://doi.org/10.1016/j.jmapro.2022.11.057.
[23] Khan S, Joshi K, Deshmukh S. A comprehensive review on effect of printing parameters on mechanical properties of FDM printed parts. Mater Today Proc 2022;50:2119–27. https://doi.org/10.1016/j.matpr.2021.09.433.
[24] Benamira M, Benhassine N, Ayad A, Dekhane A. Investigation of printing parameters effects on mechanical and failure properties of 3D printed PLA. Eng Fail Anal 2023;148:107218. https://doi.org/10.1016/j.engfailanal.2023.107218.
[25] Khosravani MR, Berto F, Ayatollahi MR, Reinicke T. Characterization of 3D-printed PLA parts with different raster orientations and printing speeds. Sci Rep 2022;12(1):1016. https://doi.org/10.1038/s41598-022-05005-4.
[26] Buj-Corral I, Bagheri A, Domínguez-Fernández A, Casado-López R. Influence of infill and nozzle diameter on porosity of FDM printed parts with rectilinear grid pattern. Procedia Manuf 2019;41:288–95. https://doi.org/10.1016/j.promfg.2019.09.011.
[27] Qamar Tanveer MD, Mishra G, Mishra S, Sharma R. Effect of infill pattern and infill density on mechanical behaviour of FDM 3D printed Parts- a current review. Mater Today Proc 2022;62:100–8. https://doi.org/10.1016/j.matpr.2022.02.310.
[28] Garmabi MM, Shahi P, Tjong J, Sain M. 3D printing of polyphenylene sulfide for functional lightweight automotive component manufacturing through enhancing interlayer bonding. Addit Manuf 2022;56:102780. https://doi.org/10.1016/j.addma.2022.102780.
[29] Ahmadifar M, Benfriha K, Shirinbayan M, Fitoussi J, Tcharkhtchi A. Mechanical behavior of polymer-based composites using fused filament fabrication under monotonic and fatigue loadings. Polymer and Polymer Composites 2022;30:1–11. https://doi.org/10.1177/09673911221082480.
[30] Ahmadifar M, Shirinbayan M, Benfriha K. Investigation of the impact of the short fiber reinforcements on the thermal and mechanical properties of polymer-based

composites manufactured by material extrusion. Int J Adv Manuf Technol 2023; 127:3801–17. https://doi.org/10.1007/s00170-023-11758-7.
[31] Ahmadifar M, Benfriha K, Shirinbayan M. Thermal, tensile and fatigue behaviors of the PA6, short carbon fiber-reinforced PA6, and continuous glass fiber-reinforced PA6 materials in fused filament fabrication (FFF). Polymers 2023;15(3):507. https://doi.org/10.3390/polym15030507.
[32] Subramaniyan M, Karuppan S, Appusamy A, Pitchandi N. Sandwich printing of PLA and carbon fiber reinforced-PLA for enhancing tensile and impact strength of additive manufactured parts. J Manuf Processes 2025;137:425–36. https://doi.org/10.1016/j.jmapro.2025.02.001.
[33] Brenken B, Favaloro A, Kunc V, Pipes RB. Fused filament fabrication of fiber-reinforced polymers: a review. Addit Manuf 2018;21:1–16. https://doi.org/10.1016/j.addma.2018.01.002.
[34] Kabir SMF, Mathur K, Seyan AFM. A critical review on 3D printed continuous fiber-reinforced composites: history, mechanism, materials and properties. Compos Struct 2020;232:111476. https://doi.org/10.1016/j.compstruct.2019.111476.
[35] Naranjo-Lozada J, Ahuett-Garza H, Orta-Castañón P, Verbeeten WMH, Sáiz-González D. Tensile properties and failure behavior of chopped and continuous carbon fiber composites produced by additive manufacturing. Addit Manuf 2019; 26:227–41. https://doi.org/10.1016/j.addma.2018.12.020.
[36] Matsuzaki R, Ueda M, Namiki M, Jeong TK, Asahara H, Horiguchi K, et al. Three-dimensional printing of continuous-fiber composites by in-nozzle impregnation. Sci Rep 2016;6(1):23058. https://doi.org/10.1038/srep23058.
[37] van de Werken N, Ghorbani J, Doyle D, Tehrani M. Investigating the hot isostatic pressing of an additively manufactured continuous carbon fiber reinforced PEEK composite. Addit Manuf 2021;37:101634. https://doi.org/10.1016/j.addma.2020.101634.
[38] Abualbandora TA, Alshneeqat MG, Mourad AHI. Impact of 3D printing parameters of short carbon fiber reinforced polymer CFRP on the mechanical and failure performance: review and future perspective. Next Mater 2025;8:100645. https://doi.org/10.1016/j.nxmate.2025.100645.
[39] Tian X, Liu T, Yang C, Wang Q, Li D. Interface and performance of 3D printed continuous carbon fiber reinforced PLA composites. Composites, Part A 2016;88: 198–205. https://doi.org/10.1016/j.compositesa.2016.05.032.
[40] Zhu W, Fu L, Tian X, Zhi Q, Hou Z, Zhang Z, et al. Three-dimensional printing of high-performance continuous fiber-reinforced thermoplastic composites: causes and elimination of process-induced defects. Composites Part B 2025;292:112080. https://doi.org/10.1016/j.compositesb.2024.112080.
[41] Hu Y, Ladani RB, Brandt M, Li Y, Mouritz AP. Carbon fibre damage during 3D printing of polymer matrix laminates using the FDM process. Mater Des 2021;205: 109679. https://doi.org/10.1016/j.matdes.2021.109679.
[42] Parker M, Ezeokeke N, Matsuzaki R, Arola D. Strength and its variability in 3D printing of polymer composites with continuous fibers. Mater Des 2023;225: 111505. https://doi.org/10.1016/j.matdes.2022.111505.
[43] Bettini P, Alitta G, Sala G, Di Landro L. Fused deposition technique for continuous fiber reinforced thermoplastic. J Mater Eng Perform 2017;26(2):843–8. https://doi.org/10.1007/s11665-016-2459-8.
[44] Ding S, Zou B, Lui Q, Wang X, Jikai L, Li L. Non-planar additive manufacturing of pre-impregnated continuous fiber reinforced composites using a three-axis printer. J Mater Res Technol 2024;32:4410–9. https://doi.org/10.1016/j.jmrt.2024.09.032.
[45] Cai H, Chen Y. A review of print heads for fused filament fabrication of continuous carbon fiber-reinforced composites. Micromachines 2024;15(4):432. https://doi.org/10.3390/mi15040432.
[46] Cheng P, Han Z, Chen Y, Ye L. Recent progress in non-planar 3D printing of continuous fiber-reinforced composites. Composites, Part A 2025;194:108900. https://doi.org/10.1016/j.compositesa.2025.108900.
[47] Tuli NT, Khatun S, Rashid AB. Unlocking the future of precision manufacturing: a comprehensive exploration of 3D printing with fiber-reinforced composites in aerospace, automotive, medical, and consumer industries. Heliyon 2024;10(5): e27328. https://doi.org/10.1016/j.heliyon.2024.e27328.
[48] Shuto R, Norimatsu S, Arola D, Matsuzaki R. Effect of the nozzle temperature on the microstructure and interlaminar strength in 3D printing of carbon fiber/polyphenylene sulfide composites. Composites, Part C 2022;9:100328. https://doi.org/10.1016/j.jcomc.2022.100328.
[49] Parker M, Inthavong A, Law E, Waddell S, Ezeokeke N, Matsuzaki R, et al. 3D printing of continuous carbon fiber reinforced polyphenylene sulfide: exploring printability and importance of fiber volume fraction. Addit Manuf 2022;54: 102763. https://doi.org/10.1016/j.addma.2022.102763.
[50] Tian X, Todoroki A, Liu T, Wu L, Hou Z, Ueda M, et al. 3D printing of continuous fiber reinforced polymer composites: development, application, and prospective. Chin J Mech Eng: Addit Manuf Front 2022;1(1):100016. https://doi.org/10.1016/j.cjmeam.2022.100016.
[51] Seon G, Makeeve A, Schaefer JD, Justusson B. Measurement of interlaminar tensile strength and elastic properties of composites using open-hole compression testing and digital image correlation. Appl Sci 2019;9(13):2647. https://doi.org/10.3390/app9132647.
[52] Todoroki A, Osada T, Mizutani Y, Suzaki Y, Ueda M, Matsuzaki R, et al. Tensile property evaluations of 3D printed continuous carbon fiber reinforced thermoplastic composites. Adv Compos Mater 2019;29(2):147–62. https://doi.org/10.1080/09243046.2019.1650323.
[53] Fitzharris ER, Rosen DW, Shofner ML. Fast scanning calorimetry for semicrystalline polymers in fused deposition modeling. Polymer 2019;166:196–205. https://doi.org/10.1016/j.polymer.2019.01.083.
[54] Oshima S, Higuchi R, Kato M, Minakuchi S, Yokozeki T, Aoki T. Cooling rate-dependent mechanical properties of polyphenylene sulfide (PPS) and carbon fiber reinforced PPS (CF/PPS). Composites, Part A 2023;164:107250. https://doi.org/10.1016/j.compositesa.2022.107250.